Stochastic Environmental Research and Risk Assessment
https://doi.org/10.1007/s00477-020-01855-4

ORIGINAL PAPER

A spectral algorithm to simulate nonstationary random fields on spheres and multifractal star-shaped random sets

Xavier Emery[1,2] · Alfredo Alegría[3]

Abstract
An extension of the turning arcs algorithm is proposed for simulating a random field on the two-dimensional sphere with a second-order dependency structure associated with a locally varying Schoenberg sequence. In particular, the correlation range as well as the fractal index of the simulated random field, obtained as a weighted sum of Legendre waves with random degrees, may vary from place to place on the spherical surface. The proposed algorithm is illustrated with numerical examples, a by-product of which is a closed-form expression for two new correlation functions (exponential-Bessel and hypergeometric models) on the sphere, together with their respective Schoenberg sequences. The applicability of our findings is also described via the emulation of three-dimensional multifractal star-shaped random sets.

Keywords Anisotropic covariance function · Hausdorff dimension · Multifractal · Schoenberg sequence · Turning Arcs

1 Introduction

Random fields on spheres are employed in the natural sciences, in particular in astronomy, oceanography, geophysics, environmental and atmospheric sciences, to quantify and emulate the uncertainty associated with phenomena defined over planet Earth or over the celestial vault (Marinucci and Peccati 2011; Anh et al. 2018; Porcu et al. 2018; Alegría et al. 2019). Other applications include the modeling of direction-dependent rock mass properties in structural geology or geotechnics (Sánchez et al. 2019), as well as the modeling of rigid star-shaped objects with stochastically varying boundaries (Kent et al. 2000; Hobolth 2003; Ziegel 2013; Hansen et al. 2015).

Alegría et al. (2020) recently introduced the *turning arcs* algorithm for simulating isotropic random fields on spheres, being the analog of the turning bands method developed to simulate stationary random fields in Euclidean spaces (Matheron 1973; Mantoglou and Wilson 1982; Emery et al. 2016). While congenial, the assumption of isotropy is, however, often simplistic to represent natural phenomena distributed on the Earth, which motivates the search for nonstationary (anisotropic) random field models, i.e., random fields whose finite-dimensional distributions are not invariant under the group of rotations. One family of such models are the axially symmetric random fields (Jones 1963), which are stationary with respect to longitude but not with respect to latitude and are used to model data distributed over large portions of the Earth (Jun and Stein 2008; Porcu et al. 2019). The aim of this work is to show that the turning arcs approach can be used as a building block to construct a more general class of nonstationary random fields on the sphere, by considering spectral representations of covariance functions whose characteristics vary on the surface of the sphere. In particular, it will be shown that one can obtain random fields with locally varying smoothness properties, which allows the generation of multifractal star-shaped random sets.

The outline of the paper is the following. In Sect. 2 we review preliminary results about isotropic random fields on spheres and their fractal indices and we describe the

✉ Xavier Emery
xemery@ing.uchile.cl

[1] Department of Mining Engineering, University of Chile, Santiago, Chile

[2] Advanced Mining Technology Center, University of Chile, Santiago, Chile

[3] Departamento de Matemática, Universidad Técnica Federico Santa María, Valparaíso, Chile

Published online: 14 August 2020

construction of star-shaped random sets. In Sect. 3 we propose a general framework to construct random fields with locally adaptive second-order dependency structures. Additionally, we look at the connections between our formulation and a kernel-based technique. In Sect. 4 we introduce a simulation algorithm based on a weighted sum of Legendre polynomial waves and we present numerical examples to assess its performance. In addition, we illustrate the applicability of our findings in the emulation of multifractal star-shaped random particles. Section 5 presents the conclusions of the paper and perspectives for future work.

Throughout the remainder of the paper, the covariance structure of the nonstationary random field targeted for simulation and its spectral representation (Schoenberg sequence) are assumed to be known beforehand. For instance, the covariance model can be inferred from a set of experimental data with an adaptation to the sphere of the approach proposed by Fouedjio et al. (2016) in the Euclidean space, which consists in (1) estimating locally isotropic covariance functions by a kernel moment method at a set of anchor locations distributed over the sphere (e.g., at regularly spaced latitudes and longitudes), (2) estimating the covariance parameters at each anchor location by least squares optimization, given a parametric family of covariance models, and (3) estimating the covariance parameters at each target location on the sphere by kernel regression from the parameters estimated at the anchor locations.

2 Background

2.1 Isotropic random fields on spheres

Consider the unit 2-sphere embedded in $\mathbb{R}^3$, denoted by $\mathbb{S}^2 = \{\boldsymbol{x} \in \mathbb{R}^3 : \|\boldsymbol{x}\| = 1\}$, with $\|\cdot\|$ representing the Euclidean norm. Let $\{Z(\boldsymbol{x}) : \boldsymbol{x} \in \mathbb{S}^2\}$ be a real-valued second-order random field, with mean function $\mu(\boldsymbol{x}) = \mathbb{E}\{Z(\boldsymbol{x})\}$, $\boldsymbol{x} \in \mathbb{S}^2$, and covariance function $C(\boldsymbol{x}_1, \boldsymbol{x}_2) = \mathrm{cov}\{Z(\boldsymbol{x}_1), Z(\boldsymbol{x}_2)\}$, $\boldsymbol{x}_1, \boldsymbol{x}_2 \in \mathbb{S}^2$. The random field is (weakly) stationary or (weakly) isotropic (Marinucci and Peccati 2011) if it has a constant mean and if its covariance function is of the form

$$C(\boldsymbol{x}_1, \boldsymbol{x}_2) = K\{d(\boldsymbol{x}_1, \boldsymbol{x}_2)\}, \quad \boldsymbol{x}_1, \boldsymbol{x}_2 \in \mathbb{S}^2, \tag{1}$$

for some continuous function $K : [0, \pi] \to \mathbb{R}$, where $d(\boldsymbol{x}_1, \boldsymbol{x}_2) = \arccos\{\boldsymbol{x}_1^\top \boldsymbol{x}_2\} \in [0, \pi]$ is the geodesic (or great-circle) distance on $\mathbb{S}^2$. Thus, $C(\boldsymbol{x}_1, \boldsymbol{x}_2)$ is only a function of the geodesic distance between locations. Following Guella and Menegatto (2018), we call K the *isotropic part* of C.

A given function is an admissible covariance function if and only if it is *positive semidefinite*, that is, for all $k \in \mathbb{N}^*$, and for all collection of locations $\boldsymbol{x}_1, \ldots, \boldsymbol{x}_k \in \mathbb{S}^2$ and scalars $a_1, \ldots, a_k \in \mathbb{R}$,

$$\mathrm{var}\left\{\sum_{i=1}^{k} a_i Z(\boldsymbol{x}_i)\right\} = \sum_{i=1}^{k}\sum_{j=1}^{k} a_i a_j C(\boldsymbol{x}_i, \boldsymbol{x}_j) \geq 0. \tag{2}$$

A classical result provided by Schoenberg (1942) states that C as in (1) is positive semidefinite if and only if its isotropic part K can be written as

$$K(d) = \sum_{n=0}^{\infty} b_n P_n(\cos d), \quad 0 \leq d \leq \pi, \tag{3}$$

where the shortcut d is used to represent the geodesic distance. Here, P_n is the Legendre polynomial of degree n (Olver et al. 2010, table 18.3.1), and $\{b_n : n \in \mathbb{N}\}$ is a sequence of nonnegative coefficients such that $\sum_{n=0}^{\infty} b_n < \infty$. As in Gneiting (2013), we refer to this sequence as a *Schoenberg sequence*. Standard inversion formulae yield

$$b_n = \frac{2n+1}{2} \int_0^{\pi} P_n(\cos \xi) \sin(\xi) K(\xi) \mathrm{d}\xi, \quad n \in \mathbb{N}.$$

While Gneiting (2013) supplied an extensive catalog of parametric families of covariance functions for isotropic random fields on spheres, other authors including Guinness and Fuentes (2016) and Alegria et al (2018) focused on parametric models for the Schoenberg sequence, which fully characterizes the isotropic covariance function.

2.2 Fractal index

The level of smoothness or roughness of the sample paths of an isotropic random field depends on the asymptotic behavior of the isotropic part K near zero. The fractal index provides a quantitative measure of this aspect of the random field. Recent literature about this topic can be found in Hansen et al. (2015), Lang and Schwab (2015), Cheng and Xiao (2016) and Guinness and Fuentes (2016).

Formally, a random field with covariance function as in (1) has fractal index $\alpha > 0$ if

$$K(0) - K(d) \sim c_0 d^{\alpha}, \tag{4}$$

as $d \searrow 0$, for some constant $c_0 > 0$. Here, for two functions f and g, $f(d) \sim g(d)$ as $d \searrow 0$ if and only if

$$\lim_{d \to 0} f(d)/g(d) = 1.$$

The fractal index has been calculated for several parametric classes of covariance functions. It is always true that $0 < \alpha \leq 2$, where $\alpha = 2$ and $\alpha \to 0$ represent the cases of

extreme smoothness and extreme roughness of the sample paths, respectively.

Abelian and Tauberian theorems (Bingham 1978; Malyarenko 2004) connect the asymptotic behavior of K near zero to that of its Schoenberg sequence near infinity. Hence, the fractal index can be alternatively specified through the decay of the Schoenberg sequence. A function $f : (0,\infty) \to (0,\infty)$ is said to be *slowly varying* at infinity if, for every $r > 0$,

$$\lim_{t\to\infty} \frac{f(rt)}{f(t)} = 1.$$

Then, Malyarenko (2004) shows that, for $0 < \alpha < 2$,

$$K(0) - K(d) \sim 2^{-\alpha} d^{\alpha} f(1/d), \tag{5}$$

as $d \searrow 0$, if, and only if,

$$\sum_{k=n}^{\infty} b_k \sim f(n) n^{-\alpha}, \tag{6}$$

as $n \to \infty$. While the implication (6)⇒(5) is called an Abelian theorem, the converse is called a Tauberian theorem.

2.3 Star-shaped random sets

The accurate modeling of three-dimensional star-shaped particles has attracted interest in many branches of knowledge such as astronomy, material science and medicine (Stoyan and Stoyan 1994). The Hausdorff (or fractal) dimension, a concept arising from the study of irregular shapes, plays a fundamental role in the analysis of solid particles because it serves as a valuable mathematical tool to quantify the degree of smoothness or roughness of the surface of the particle. Recent findings indicate that fractal geometry is a convenient tool for describing the topography of astronomical bodies in the solar system (Kucinskas et al. 1992), the mechanisms of tumor growth and angiogenesis (Sedivy and Mader 1997), as well as the morphology of sand grains (Zhou et al. 2017).

Formally, a particle is represented as a closed and bounded set $Y \subset \mathbb{R}^3$, being star-shaped with respect to an interior point $\boldsymbol{o}$, i.e., for each $\boldsymbol{x} \in Y$, the whole line segment joining $\boldsymbol{o}$ and $\boldsymbol{x}$ is contained in Y. The set Y can be completely characterized in terms of its radial function, defined as $Z(\boldsymbol{x}) = \max\{r \geq 0 : \boldsymbol{o} + r\boldsymbol{x} \in Y\}$, for $\boldsymbol{x} \in \mathbb{S}^2$. Accordingly, Y can be represented as

$$Y = \bigcup_{\boldsymbol{x}\in\mathbb{S}^2} \{\boldsymbol{o} + r\boldsymbol{x} : 0 \leq r \leq Z(\boldsymbol{x})\}.$$

Adopting the framework presented by Hansen et al. (2015), the radial function $Z(\boldsymbol{x})$ is modeled as a Gaussian random field on $\mathbb{S}^2$. Since $Z(\boldsymbol{x})$ may take negative values, $Z(\boldsymbol{x})$ could be replaced with $Z_c(\boldsymbol{x}) = \max\{c, Z(\boldsymbol{x})\}$ for some $c > 0$, or with another transform that ensures positiveness. Throughout, the interior point $\boldsymbol{o}$ is assumed to be the origin.

The Hausdorff dimension (Adler 1981) allows quantifying the regularity of the surface of Y. A formal definition in terms of ball coverings (Hansen et al. 2015) is given now. For $\epsilon > 0$, an ϵ-cover of Y is a countable collection $\{B_i : i = 1, 2, \ldots\}$ of balls $B_i \subset \mathbb{R}^3$ of diameter $|B_i|$ less than or equal to ϵ that covers Y. Let

$$H^{\eta}(Y) = \lim_{\epsilon\to 0} \inf\Bigg\{ \sum_{i=1}^{\infty} |B_i|^{\eta} : \{B_i : i = 1, 2, \ldots\} \text{ is an } \epsilon\text{-cover of } Y \Bigg\},$$

where the infimum is taken over all the ϵ-covers of Y, be the η-dimensional Hausdorff measure of Y. The Hausdorff dimension of Y is the unique nonnegative number η_0 such that $H^{\eta}(Y) = \infty$ if $\eta < \eta_0$ and $H^{\eta}(Y) = 0$ if $\eta > \eta_0$.

In the special case when $Z(\boldsymbol{x})$ is isotropic, Hansen et al. (2015) showed that $\eta_0 = 3 - \alpha/2$ almost surely, where α is the fractal index of $Z(\boldsymbol{x})$ defined in (4), which implies that $2 \leq \eta_0 < 3$. For sets with conventional smooth shapes, the Hausdorff dimension matches the ordinary topological dimension $\eta_0 = 2$. In contrast, as the Hausdorff dimension increases, the set becomes more and more irregular.

3 Nonstationary random fields on spheres

3.1 Spatially adaptive Schoenberg sequences

The aim of this section is to propose a general framework for the construction of nonstationary random field models on spheres. The following proposition provides a simple and general approach to escape from isotropy, based on spatially adaptive Schoenberg sequences.

Proposition 1 *Let $\{\beta_n(\boldsymbol{x}_1, \boldsymbol{x}_2) : n \in \mathbb{N}\}$ be a sequence of positive semidefinite functions on $\mathbb{S}^2 \times \mathbb{S}^2$, such that $\sum_{n=0}^{\infty} \beta_n(\boldsymbol{x}, \boldsymbol{x}) < \infty$, for every $\boldsymbol{x} \in \mathbb{S}^2$. Thus,*

$$C(\boldsymbol{x}_1, \boldsymbol{x}_2) = \sum_{n=0}^{\infty} \beta_n(\boldsymbol{x}_1, \boldsymbol{x}_2) P_n(\boldsymbol{x}_1^{\top}\boldsymbol{x}_2), \quad \boldsymbol{x}_1, \boldsymbol{x}_2 \in \mathbb{S}^2, \tag{7}$$

is a positive semidefinite function.

The proof of Proposition 1 is deferred to Appendix A. We call the sequence of functions $\{\beta_n(\boldsymbol{x}_1, \boldsymbol{x}_2) : n \in \mathbb{N}\}$ an *adaptive Schoenberg sequence*. Equation (7) is a convenient construction because when both $\boldsymbol{x}_1$ and $\boldsymbol{x}_2$ are near some fixed location $\boldsymbol{x}_0 \in \mathbb{S}^2$, and β_n is a sufficiently smooth function, for each $n \in \mathbb{N}$, one has

$$C(\boldsymbol{x}_1,\boldsymbol{x}_2) \approx \sum_{n=0}^{\infty} \beta_n(\boldsymbol{x}_0,\boldsymbol{x}_0) P_n(\boldsymbol{x}_1^\top \boldsymbol{x}_2), \quad \boldsymbol{x}_1,\boldsymbol{x}_2 \in \mathbb{S}^2.$$

Consequently, covariance functions with locally isotropic behaviors are possible, making this class of models versatile and attractive. In particular, the correlation range and the fractal index of the random field can vary on the spherical surface. A similar construction principle, based on a Fourier series representation, has been adopted by Porcu et al. (2019) to model global temperatures. For simplicity, from now on we pay attention to constructions of the form

$$\begin{aligned} C(\boldsymbol{x}_1,\boldsymbol{x}_2) = &\sum_{n=0}^{\infty} \{b_n(\boldsymbol{x}_1) b_n(\boldsymbol{x}_2)\}^{1/2} \\ &\times P_n(\boldsymbol{x}_1^\top \boldsymbol{x}_2), \quad \boldsymbol{x}_1,\boldsymbol{x}_2 \in \mathbb{S}^2, \end{aligned} \tag{8}$$

with b_n being a nonnegative function on $\mathbb{S}^2$. This choice is a special case of (7), and is sufficiently general to achieve models with flexible local ranges and fractal properties. Actually, the proposed model is capable of emulating kernel-based covariance functions, which are widely used in the spatial analysis literature (Nott and Dunsmuir 2002; Heaton et al. 2014). Indeed, in a kernel-based approach, the random field $Z(\boldsymbol{x})$ on $\mathbb{S}^2$ is written as a spatially weighted combination of isotropic random fields. This strategy allows modeling dissimilar local dependency structures in different spatial zones. Let $D_1,\ldots,D_J$ be a collection of subregions that cover $\mathbb{S}^2$, and let $\lambda_j(d(\boldsymbol{x},\overline{\boldsymbol{x}}_j))$ be a positive geodesic kernel function centered at the centroid $\overline{\boldsymbol{x}}_j$ of D_j, for all $j = 1,\ldots,J$ (see (Schreiner 1997)). Consider the random field

$$Z(\boldsymbol{x}) = \sum_{j=1}^{J} \lambda_j(d(\boldsymbol{x},\overline{\boldsymbol{x}}_j)) Z_j(\boldsymbol{x}), \quad \boldsymbol{x} \in \mathbb{S}^2,$$

where $Z_1(\boldsymbol{x}),\ldots,Z_J(\boldsymbol{x})$ is a collection of independent isotropic random fields on $\mathbb{S}^2$. Suppose that the covariance function of $Z_j(\boldsymbol{x})$ has isotropic part K_j. Thus, $Z(\boldsymbol{x})$ has the following covariance function

$$\begin{aligned} C(\boldsymbol{x}_1,\boldsymbol{x}_2) = &\sum_{j=1}^{J} \lambda_j(d(\boldsymbol{x}_1,\overline{\boldsymbol{x}}_j)) \lambda_j(d(\boldsymbol{x}_2,\overline{\boldsymbol{x}}_j)) \\ &\times K_j\{d(\boldsymbol{x}_1,\boldsymbol{x}_2)\}, \quad \boldsymbol{x}_1,\boldsymbol{x}_2 \in \mathbb{S}^2. \end{aligned} \tag{9}$$

Since K_j admits a representation of the form $K_j(d) = \sum_{n=0}^{\infty} p_{n,j} P_n(\cos d)$, for each $j = 1,\ldots,J$, where $\{p_{n,j} : n \in \mathbb{N}\}$ is the associated jth Schoenberg sequence, the covariance function (9) can be written as

$$\begin{aligned} C(\boldsymbol{x}_1,\boldsymbol{x}_2) = &\sum_{j=1}^{J} \sum_{n=0}^{\infty} \lambda_j(d(\boldsymbol{x}_1,\overline{\boldsymbol{x}}_j)) \lambda_j(d(\boldsymbol{x}_2,\overline{\boldsymbol{x}}_j)) \\ &\times p_{n,j} P_n(\boldsymbol{x}_1^\top \boldsymbol{x}_2), \quad \boldsymbol{x}_1,\boldsymbol{x}_2 \in \mathbb{S}^2. \end{aligned} \tag{10}$$

We observe that (10) can be obtained as the sum of J covariance functions of the form (8), where the jth adaptive Schoenberg sequence in (8) is constructed from $b_{n,j}(\boldsymbol{x}) = \lambda_j^2(d(\boldsymbol{x},\overline{\boldsymbol{x}}_j)) p_{n,j}$.

In the following subsections, we provide a few examples of isotropic correlation functions, i.e., covariance functions that only depend on the geodesic distance and have a unit variance at each point of the sphere ($C(\boldsymbol{x},\boldsymbol{x}) = \sum_{n=0}^{+\infty} b_n = 1$ for any $\boldsymbol{x} \in \mathbb{S}^2$), and their generalization to nonstationary (anisotropic) correlation functions constructed on the basis of adaptive Schoenberg sequences.

3.2 Example 1: Legendre–Matérn model

The isotropic Legendre–Matérn correlation function (Guinness and Fuentes 2016) is characterized by the Schoenberg sequence

$$b_n = S(a,\nu,0)^{-1} (a^2+n^2)^{-\nu-1/2}, \quad n \in \mathbb{N}, \tag{11}$$

where $a > 0$, $\nu > 0$ and $S(a,\nu,p) = \sum_{k=p}^{+\infty} (a^2+k^2)^{-\nu-1/2}$. While a regulates the practical range (the distance at which the correlation function reaches a given threshold) of the random field, ν controls the smoothness of the sample paths. Indeed, since $S(a,\nu,n) \sim n^{-2\nu}(2\nu)^{-1}$ as $n \to \infty$, we conclude from Malyarenko's characterization that, for $0 < \nu < 1$, the associated random field has fractal index $\alpha = 2\nu$. For $\nu > 1$ the random field is differentiable in a mean square sense, in which case the fractal index is $\alpha = 2$, and we refer the reader to Guinness and Fuentes (2016) for details. The previous results can be extended to the limit case $\nu = 1$, which also yields a fractal index equal to 2 (Bingham 1978).

A natural extension of the Legendre–Matérn model (11) is obtained from the adaptive Schoenberg representation (8), by considering

$$\begin{aligned} b_n(\boldsymbol{x}) = &S(a(\boldsymbol{x}),\nu(\boldsymbol{x}),0)^{-1} \\ &\times (a(\boldsymbol{x})^2+n^2)^{-\nu(\boldsymbol{x})-1/2}, \quad n \in \mathbb{N}, \quad \boldsymbol{x} \in \mathbb{S}^2, \end{aligned} \tag{12}$$

where ν and a are positive functions controlling the locally varying fractal index and practical range of the sample paths, respectively. In what follows, we call (12) the adaptive Legendre–Matérn model.

3.3 Example 2: multiquadric model

The isotropic multiquadric correlation function and its associated Schoenberg sequence are (Gneiting 2013; Moller et al. 2018; Peron et al. 2018)

$$C(\boldsymbol{x}_1,\boldsymbol{x}_2) = \frac{1-a}{(1+a^2-2a\,\boldsymbol{x}_1^\top\boldsymbol{x}_2)^{\frac{1}{2}}}, \quad \boldsymbol{x}_1,\boldsymbol{x}_2 \in \mathbb{S}^2, \tag{13}$$

and

$$b_n = (1-a)\,a^n, \quad n \in \mathbb{N}, \tag{14}$$

with $a \in (0,1)$. According to criterion (4), the fractal index of this model is $\alpha = 2$, which means that the sample paths are very smooth. As a increases, the practical range decreases, implying spatial variations at a shorter scale. As for the previous example, an adaptive model is defined by considering spatially-varying coefficients:

$$b_n(\boldsymbol{x}) = (1-a(\boldsymbol{x}))\,a(\boldsymbol{x})^n, \quad n \in \mathbb{N}. \tag{15}$$

The corresponding nonstationary correlation function (8) has the following closed-form expression:

$$C(\boldsymbol{x}_1,\boldsymbol{x}_2) = \left(\frac{(1-a(\boldsymbol{x}_1))\,(1-a(\boldsymbol{x}_2))}{1+a(\boldsymbol{x}_1)\,a(\boldsymbol{x}_2)-2\sqrt{a(\boldsymbol{x}_1)\,a(\boldsymbol{x}_2)}\boldsymbol{x}_1^\top\boldsymbol{x}_2}\right)^{\frac{1}{2}}. \tag{16}$$

3.4 Example 3: exponential-Bessel model

The isotropic exponential-Bessel correlation function is given by:

$$C(\boldsymbol{x}_1,\boldsymbol{x}_2) = \exp\big(a\,(\boldsymbol{x}_1^\top\boldsymbol{x}_2-1)\big) \times J_0\left(a\sqrt{1-(\boldsymbol{x}_1^\top\boldsymbol{x}_2)^2}\right), \tag{17}$$

where $a > 0$ and J_0 is the zeroth order Bessel function of the first kind (Olver et al. 2010, formula 10.2.2). Such a correlation function has a fractal index equal to 2, as per criterion (4), hence it is associated with smooth sample paths; the practical range and scale of variations are controlled by parameter a (the larger a, the smaller the practical range). The isotropic part of $C(\boldsymbol{x}_1,\boldsymbol{x}_2)$, as defined in 1, takes negative values on some subset of $(0,\pi)$ if a is greater than 1.7005, is nonmonotonic (i.e., it has a hole effect) if a is greater than 2.7094, and presents damped oscillations if a is greater than 4.9608. An explicit expression of the Schoenberg sequence can be deduced from formula 18.12.12 of Olver et al. (2010):

$$b_n = \exp(-a)\,\frac{a^n}{n!}, \quad n \in \mathbb{N}, \tag{18}$$

which is positive and summable, ensuring the positive semidefiniteness of $C(\boldsymbol{x}_1,\boldsymbol{x}_2)$. The extension to a nonstationary model is straightforward, by considering the sequence

$$b_n(\boldsymbol{x}) = \exp(-a(\boldsymbol{x}))\,\frac{a(\boldsymbol{x})^n}{n!}, \quad n \in \mathbb{N}, \tag{19}$$

with a a positive function. This leads to a correlation function of the form

$$C(\boldsymbol{x}_1,\boldsymbol{x}_2) = \exp\left(\sqrt{a(\boldsymbol{x}_1)a(\boldsymbol{x}_2)}\,\boldsymbol{x}_1^\top\boldsymbol{x}_2 - \frac{a(\boldsymbol{x}_1)+a(\boldsymbol{x}_2)}{2}\right) \times J_0\left(\sqrt{a(\boldsymbol{x}_1)a(\boldsymbol{x}_2)(1-(\boldsymbol{x}_1^\top\boldsymbol{x}_2)^2)}\right). \tag{20}$$

3.5 Example 4: hypergeometric model

The isotropic hypergeometric correlation function is

$$C(\boldsymbol{x}_1,\boldsymbol{x}_2) = \left(\frac{1-a}{1-a\,\boldsymbol{x}_1^\top\boldsymbol{x}_2}\right)^{\nu} {}_2F_1 \times \left(\frac{\nu}{2},\frac{\nu+1}{2};1;a^2\,\frac{(\boldsymbol{x}_1^\top\boldsymbol{x}_2)^2-1}{(1-a\,\boldsymbol{x}_1^\top\boldsymbol{x}_2)^2}\right), \tag{21}$$

where $a \in (0,1)$, $\nu > 0$ and where ${}_2F_1$ is the Gauss hypergeometric function (Olver et al. 2010, formula 15.2.1). This correlation function is associated with the following Schoenberg sequence (Brafman 1951):

$$b_n = (1-a)^{\nu}\,(\nu)_n\,\frac{a^n}{n!}, \quad n \in \mathbb{N}, \tag{22}$$

where $(\nu)_n$ stands for the Pochhammer symbol (Olver et al. 2010, formula 5.2.5). Stirling's formula (Olver et al. 2010, formula 5.11.3) shows that the generic term b_n behaves like $a^n\,n^{\nu-1}$ as n tends to infinity, hence the positive series $\{b_n : n \in \mathbb{N}\}$ converges and the correlation function (21) is well-defined. As for the previous two examples, the application of criterion (4) provides a fractal index $\alpha = 2$, with a constant c_0 that increases with a and ν. Accordingly, larger parameters a and ν are associated with shorter scales of variations and a smaller practical range.

An adaptive hypergeometric model is obtained by letting a and ν vary with $\boldsymbol{x}$. If $\nu = 1$ (independent of $\boldsymbol{x}$), one has ${}_2F_1\left(\frac{1}{2},1;1;z\right) = (1-z)^{-1/2}$ (Olver et al. 2010, formula 15.4.6) and the model boils down to the multiquadric model (15). Another particular case with a simple closed-form expression is obtained when $\nu = 2$:

$$C(\boldsymbol{x}_1,\boldsymbol{x}_2) = \frac{(1-a(\boldsymbol{x}_1))^{\frac{\nu}{2}}\,(1-a(\boldsymbol{x}_2))^{\frac{\nu}{2}}\,(1-\sqrt{a(\boldsymbol{x}_1)\,a(\boldsymbol{x}_2)}\boldsymbol{x}_1^\top\boldsymbol{x}_2)}{\left(1+a(\boldsymbol{x}_1)\,a(\boldsymbol{x}_2)-2\sqrt{a(\boldsymbol{x}_1)\,a(\boldsymbol{x}_2)}\boldsymbol{x}_1^\top\boldsymbol{x}_2\right)^{\frac{3}{2}}}. \tag{23}$$

4 Simulation of adaptive models

4.1 Proposed algorithm

The following proposition provides an algorithm to simulate basic nonstationary random fields on spheres with a correlation structure of the form (8), requiring only the knowledge of the adaptive Schoenberg sequence.

Proposition 2 *Let ε be a random variable with zero mean and unit variance, $\boldsymbol{\omega}$ be a random vector uniformly distributed on $\mathbb{S}^2$, and κ be a discrete random variable with $\mathbb{P}(\kappa = n) = \zeta_n$, $n \in \mathbb{N}$, where $\mathbb{P}$ stands for the probability and where the support of the probability mass sequence $\{\zeta_n : n \in \mathbb{N}\}$ contains the support of the sequence $\{b_n(\boldsymbol{x}) : n \in \mathbb{N}\}$, for all $\boldsymbol{x} \in \mathbb{S}^2$. Suppose that ε, κ and $\boldsymbol{\omega}$ are independent. Then, the random field*

$$Z(\boldsymbol{x}) = \varepsilon \left\{ \frac{b_\kappa(\boldsymbol{x})(2\kappa+1)}{\zeta_\kappa} \right\}^{1/2} P_\kappa(\boldsymbol{\omega}^\top \boldsymbol{x}), \quad \boldsymbol{x} \in \mathbb{S}^2, \tag{24}$$

has zero mean and its covariance function is given by (8).

The proof of Proposition 2 can be found in Appendix B. In essence, (24) consists of an adequate weighted and rescaled Legendre polynomial wave. It appears as the nonstationary extension of the *turning arcs* simulation algorithm on the sphere (Alegría et al. 2020) and as the spherical extension of the continuous spectral algorithm to simulate nonstationary random fields in Euclidean spaces (Emery and Arroyo 2018). The choice of the probability mass sequence $\{\zeta_n : n \in \mathbb{N}\}$ can be made independently of the adaptive Schoenberg sequence, which is equivalent to an important sampling technique. Location and dispersion parameters can also be added in order to control the mean and variance of the sample paths.

The random field $Z(\boldsymbol{x})$ in (24) has a zero expectation and exactly the predefined second-order structure (8). One can furthermore impose that its finite-dimensional distributions are close to multivariate Gaussian by recourse to a central limit approximation, by putting

$$\widetilde{Z}(\boldsymbol{x}) = \frac{1}{L^{1/2}} \sum_{\ell=1}^{L} Z_\ell(\boldsymbol{x}), \quad \boldsymbol{x} \in \mathbb{S}^2, \tag{25}$$

where $Z_1(\boldsymbol{x}), \ldots, Z_L(\boldsymbol{x})$ are L basic random fields (Legendre waves) constructed as in (24), and L is a large integer, typically of the order of a few thousands. Several criteria have been proposed to assess the quality of the central limit approximation, based on the distributional properties of the simulated random field $\widetilde{Z}(\boldsymbol{x})$ or on the experimental properties of its sample paths. The reader is referred to the literature on the spectral-turning bands and turning arcs simulation for a thorough review of such criteria (Lantuéjoul 1994, 2002; Emery and Lantuéjoul 2006, 2008; Emery 2008; Chilès and Delfiner 2012; Emery et al. 2016; Arroyo and Emery 2017; Alegría et al. 2020). An example is presented in Sect. 4.2 and Appendix C hereunder.

The construction (25) is competitive from a computational point of view, insofar as (1) it requires a minimal memory footprint (the simulated values can be exported as soon as they are calculated), (2) it is scalable, in the sense that its overall computational cost is proportional to the number L of basic random fields and to the number $n_{\boldsymbol{x}}$ of target locations, and (3) its implementation is parallelizable. The authors are not aware of other algorithms able to exactly simulate random fields with an adaptive covariance function of the form (8) on the sphere, except the one-size-fits-all covariance matrix decomposition and sequential algorithms (Chilès and Delfiner 2012) that have a numerical complexity proportional to $n_{\boldsymbol{x}}^3$ (prohibitive when $n_{\boldsymbol{x}}$ is more than a few tens of thousands), let alone their demanding memory storage requirements.

In a similar fashion, other spectral simulation algorithms leading to random fields with a covariance of the form (8) could be designed, by adapting the constructions based on finite expansions into spherical harmonics proposed by Emery and Porcu (2019) and Lantuéjoul et al. (2019). Although these adaptations would have the same numerical complexity in $\mathcal{O}(L n_{\boldsymbol{x}})$, the calculation of spherical harmonics turns out to be much more expensive than that of Legendre polynomials, which can be obtained straightforwardly by use of recurrence relations (Olver et al. 2010, table 18.9.1). This difference in computing time would furthermore increase when generalizing the previous algorithms to higher-dimensional spheres: Legendre polynomials are then substituted by Gegenbauer polynomials (cheap to calculate) (Alegría et al. 2020), whereas spherical harmonics have to be replaced by costly hyperspherical harmonics (Emery and Porcu 2019).

In many applications, it is also of interest to condition the simulated random field to a finite set of observations scattered over the sphere. Following a standard procedure in spatial statistics, the non-conditional simulation (25) can be converted into a conditional one by means of post-conditioning kriging, see de Fouquet (1994) and Chilès and Delfiner (2012), which requires the analytical expression of the correlation function. This expression is known exactly in some cases (such as in Examples 2, 3 and 4 above), or approximately, by truncating the adaptive Schoenberg representation (8) at a high polynomial degree.

4.2 Numerical examples

For $\boldsymbol{x} \in \mathbb{S}^2$, let us denote by $\theta(\boldsymbol{x})$ its colatitude (inclination), valued between 0 and π, and by $\varphi(\boldsymbol{x})$ its longitude

(azimuth), valued between 0 and 2π, and consider the following adaptive models:

- Legendre–Matérn model with $a(\boldsymbol{x}) = 2 + 1.5\cos(\varphi(\boldsymbol{x}))$ and $\nu(\boldsymbol{x}) = 0.2 + 1.6\,\frac{\theta(\boldsymbol{x})}{\pi}$;
- multiquadric model with $a(\boldsymbol{x}) = 0.9 - 0.8\,\frac{\theta(\boldsymbol{x})}{\pi}$;
- exponential-Bessel model with $a(\boldsymbol{x}) = 8 - 7.9\,\frac{\theta(\boldsymbol{x})}{\pi}$;
- hypergeometric model with $a(\boldsymbol{x}) = 0.9 - 0.8\,\frac{\theta(\boldsymbol{x})}{\pi}$ and $\nu(\boldsymbol{x}) = 10 + 9\cos(\varphi(\boldsymbol{x}))$.

Figure 1 displays sample paths and star-shape representations of these models, obtained by using $L = 5000$ basic random fields, a Rademacher distribution for ε and a zeta distribution of parameter 2 for $\kappa + 1$:

$$\mathbb{P}(\varepsilon = -1) = \mathbb{P}(\varepsilon = 1) = \frac{1}{2},$$

$$\mathbb{P}(|\,\varepsilon\,| \neq 1) = 0$$

and

$$\mathbb{P}(\kappa = n) = \frac{6}{\pi^2\,(n+1)^2}, \quad n \in \mathbb{N}.$$

The Rademacher distribution for ε has been chosen because it leads to the smallest Berry–Esséen bound when calculating the Kolmogorov distance between the finite-dimensional distributions of the simulated random field and multivariate Gaussian distributions (Alegría et al. 2020). On the other hand, based on the fact that the support of the Schoenberg sequence is unbounded in all the models under consideration, a shifted zeta distribution has been chosen for κ because it is supported in $\mathbb{N}$ and long-tailed, hence it allows sampling a large range of polynomial degrees and reproducing both the low- and high-frequency variations of the target random field; in particular, it ensures that the Berry–Esséen bound between the marginal distribution of the simulated random field and the standard Gaussian distribution is finite and proportional to $L^{-1/2}$ (details in Appendix C). Zeta distributed random integers can be generated by recourse to an acceptance-rejection algorithm (Devroye 1986, Chapter 10).

The sample path of the adaptive Legendre–Matérn model (top left) becomes smoother and smoother as one gets farther from the north pole, which is explained because ν (therefore, the fractal index $\alpha = 2\,\min(1, \nu)$) increases with the colatitude. One can also observe that the scale of the spatial variations is not the same from east to west, which arises because a varies with the longitude. This Legendre-Matérn model offers a general strategy for modeling and simulating three-dimensional multifractal star-shaped particles, for which the Hausdorff dimension may vary from place to place on the boundary of the particle. In contrast, the simulation of isotropic random fields only implies monofractal objects (Hansen et al. 2015).

In the following two examples (multiquadric and exponential-Bessel models), a decreases with the colatitude, implying a shorter range of variations toward the north pole and a larger range of variations towards the south pole, as well as some pseudo-periodicity in the northern hemisphere in the case of the exponential-Bessel model. Both examples correspond to axially symmetric random fields, insofar as the correlation function $C(\boldsymbol{x}_1, \boldsymbol{x}_2)$ only depends on $\theta(\boldsymbol{x}_1)$, $\theta(\boldsymbol{x}_2)$ and $\varphi(\boldsymbol{x}_1) - \varphi(\boldsymbol{x}_2)$. In contrast, the last example (hypergeometric model) exhibits a range of variations that differs from north to south and from east to west, controlled by the latitudinally-varying parameter a and the longitudinally-varying parameter ν. In all these three examples, the boundary of the star-shape particle is smooth, insofar as the fractal index is constant over the sphere ($\alpha = 2$).

5 Conclusions and perspectives

We introduced a flexible framework for modeling nonstationary random fields on spheres, which are generated from a locally varying Schoenberg sequence, and proposed a computationally efficient simulation algorithm that allows reproducing exactly the second-order dependency structure. A simple locally adaptive version of the Legendre–Matérn, multiquadric, exponential-Bessel and hypergeometric covariance functions has been proposed and exemplified through numerical experiments to emulate random fields with place-to-place variable practical range and/or fractal index. In passing, the closed-form expressions of the latter two covariance functions, as well as their Schoenberg sequences, have been established. We also described the construction of multifractal star-shaped objects from our proposal.

A natural generalization of this work is to consider temporally dependent Schoenberg sequences, allowing for nonstationary random fields evolving in time. The findings of Berg and Porcu (2017) might be useful here. Another interesting problem is the search for efficient methods for estimating the covariance structure, an issue that has been left aside in this work focused on the simulation problem. In this respect, we already mentioned in the introductory section the approach proposed by Fouedjio et al. (2016) to estimate nonstationary covariance functions. Another challenging possibility is to adapt the tools reviewed in Gneiting et al. (2012), who focus on the estimation of the fractal index. Advances in this direction also include the work of Ziegel (2013).

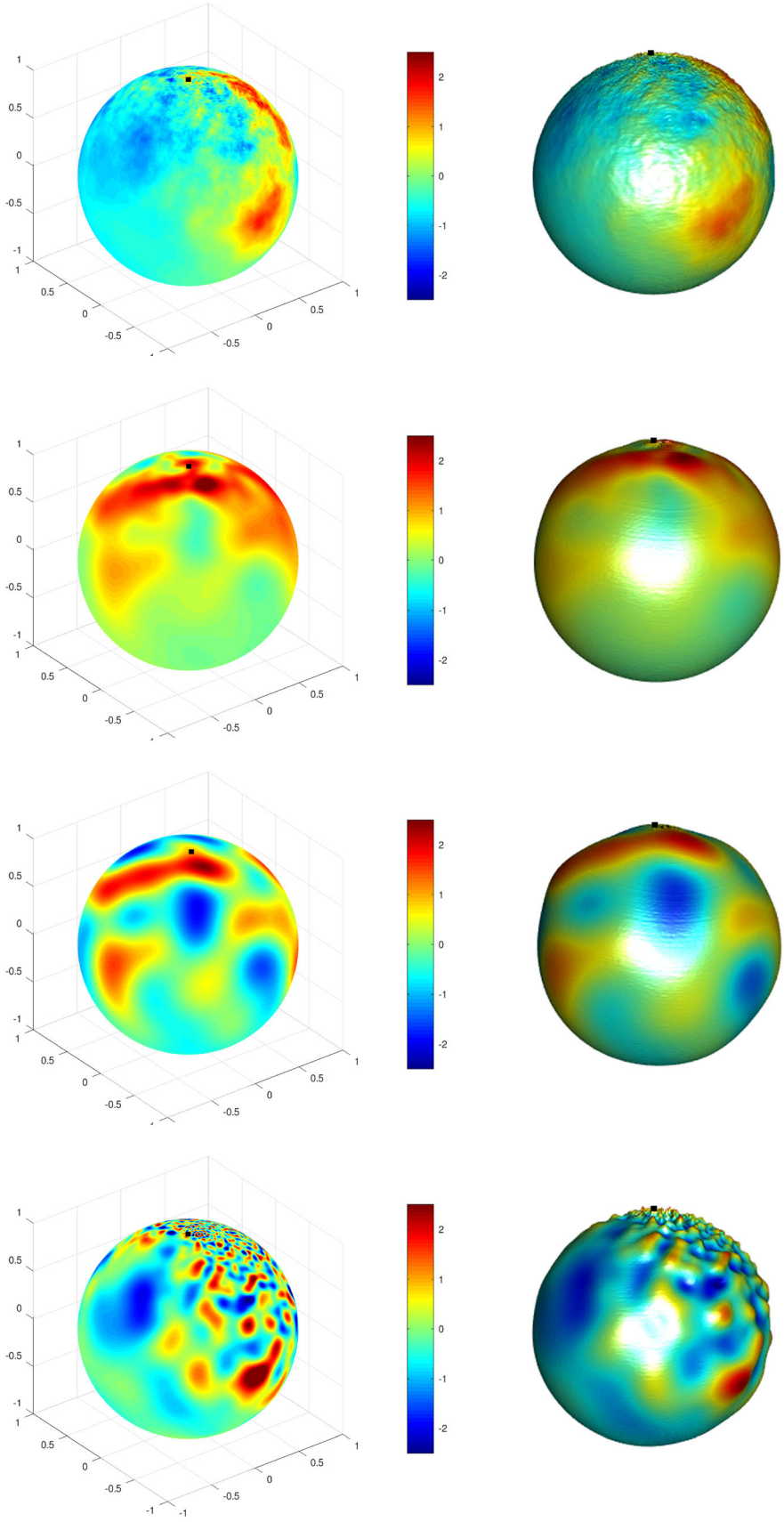

Fig. 1 Orthographic projections (left) and star-shaped representations (right) showing sample paths of nonstationary random fields with Legendre-Matérn (top row), multiquadric (second row), exponential-Bessel (third row) and hypergeometric (bottom) covariances. All these representations have been obtained by considering a discretization of the sphere into 500×500 faces and by using $L = 5000$ Legendre waves, a Rademacher distribution for ε and a zeta distribution with parameter 2 for $\kappa + 1$. A black square indicates the north pole in each representation. The radial function used in the star-shaped representations is the simulated random field increased by a constant value of 60

From a computational viewpoint, the simulation algorithm is very fast, as the number of required floating point operations is proportional to the number L of basic random fields (Legendre waves) and to the number of target locations. One may be interested in proposing an improved version of this algorithm by using high-performance computing.

According to the Open Problem 15 in Gneiting (2013), new methodologies involving nonstationary dependencies could be beneficial in environmental and climatological phenomena (see also (Castruccio and Stein 2013)). So we believe that our findings in Sect. 3 can be helpful to conduct new investigations in various fields related to spatial analysis.

Acknowledgements The authors acknowledge the funding of the National Agency for Research and Development of Chile, through grants CONICYT/FONDECYT/REGULAR/No. 1170290 (X. Emery), CONICYT PIA AFB180004 (X. Emery) and CONICYT/FONDECYT/INICIACIÓN/No. 11190686 (A. Alegría).

Appendices

A. Proof of Proposition 1

The positive semidefiniteness of (7) is a direct consequence of the *addition theorem* for spherical harmonic functions, which is described below. The set of spherical harmonic functions, $\{Y_{nm} : n \in \mathbb{N}, m = -n, \ldots, n\}$, is an orthogonal basis of the Hilbert space of complex-valued square integrable functions on $\mathbb{S}^2$. Explicit expressions for these functions can be found in Olver et al. (2010, formula 14.30.1) and Marinucci and Peccati (2011). The addition theorem for spherical harmonic functions (Olver et al. 2010, formula 14.30.9) establishes that

$$P_n(\boldsymbol{x}_1^\top \boldsymbol{x}_2) = \frac{4\pi}{2n+1} \sum_{m=0}^{n} \Big[\mathrm{Re}\{Y_{nm}(\boldsymbol{x}_1)\}\mathrm{Re}\{Y_{nm}(\boldsymbol{x}_2)\} + \mathrm{Im}\{Y_{nm}(\boldsymbol{x}_1)\}\mathrm{Im}\{Y_{nm}(\boldsymbol{x}_2)\} \Big], \quad \boldsymbol{x}_1, \boldsymbol{x}_2 \in \mathbb{S}^2,$$

where Re and Im represent real and imaginary parts, respectively. A straightforward calculation shows that, for any $k \in \mathbb{N}^*$, and for any system of points $\boldsymbol{x}_1, \ldots, \boldsymbol{x}_k \in \mathbb{S}^2$ and constants $a_1, \ldots, a_k \in \mathbb{R}$,

$$\sum_{i,j=1}^{k} a_i a_j C(\boldsymbol{x}_i, \boldsymbol{x}_j) = \sum_{i,j=1}^{k} a_i a_j \sum_{n=0}^{\infty} \beta_n(\boldsymbol{x}_i, \boldsymbol{x}_j) P_n(\boldsymbol{x}_i^\top \boldsymbol{x}_j) = \sum_{n=0}^{\infty} \frac{4\pi}{2n+1} \sum_{m=0}^{n} \Big[\sum_{i,j=1}^{k} \times \{c_{nm,i} c_{nm,j} + d_{nm,i} d_{nm,j}\} \times \beta_n(\boldsymbol{x}_i, \boldsymbol{x}_j) \Big],$$

where $c_{nm,i} = a_i \mathrm{Re}\{Y_{nm}(\boldsymbol{x}_i)\}$ and $d_{nm,i} = a_i \mathrm{Im}\{Y_{nm}(\boldsymbol{x}_i)\}$. The last expression is clearly nonnegative due to the positive semidefiniteness of the functions β_n, and the exchange order of summations is well justified by dominated convergence.

B. Proof of Proposition 2

The basic random field defined in (24) clearly has a zero expectation. On the other hand, in order to obtain its covariance function, we use the same arguments as in Alegría et al. (2020). Indeed, note that

$$\mathbb{E}\{Z(\boldsymbol{x}_1)Z(\boldsymbol{x}_2)\} = \mathbb{E}(\varepsilon^2) \sum_{n=0}^{\infty} \{b_n(\boldsymbol{x}_1) b_n(\boldsymbol{x}_2)\}^{1/2} (2n+1) \times \int_{\mathbb{S}^2} P_n(\boldsymbol{\omega}^\top \boldsymbol{x}_1) P_n(\boldsymbol{\omega}^\top \boldsymbol{x}_2) U(\mathrm{d}\boldsymbol{\omega}), \quad \boldsymbol{x}_1, \boldsymbol{x}_2 \in \mathbb{S}^2,$$

where U is the uniform probability measure on $\mathbb{S}^2$. The result follows from the duplication equation for Legendre polynomials (see, e.g., (Ziegel 2014, equation 2.4)): for any $n, k \in \mathbb{N}$,

$$\int_{\mathbb{S}^2} P_n(\boldsymbol{\omega}^\top \boldsymbol{x}_1) P_k(\boldsymbol{\omega}^\top \boldsymbol{x}_2) U(\mathrm{d}\boldsymbol{\omega}) = \frac{\delta_{n,k}}{2n+1} P_n(\boldsymbol{x}_1^\top \boldsymbol{x}_2), \quad \boldsymbol{x}_1, \boldsymbol{x}_2 \in \mathbb{S}^2,$$

where $\delta_{n,k}$ denotes the Kronecker delta.

C. Assessment of the central limit approximation

Starting with the well-known Berry–Esséen inequality, Alegría et al. (2020) showed that the Kolmogorov–Smirnov distance between the marginal distribution of $\widetilde{Z}(\boldsymbol{x})$ as defined in (25) and a Gaussian distribution is upper bounded as follows:

$$\sup_{z\in\mathbb{R}}\left|\mathbb{P}\left(\frac{\widetilde{Z}(\boldsymbol{x})}{C(\boldsymbol{x},\boldsymbol{x})^{1/2}}<z\right)-G(z)\right|\leq\frac{\xi\,\mathbb{E}(|\varepsilon|^3)}{C(\boldsymbol{x},\boldsymbol{x})^{3/2}\,L^{1/2}}$$
$$\times\sum_n\frac{b_n(\boldsymbol{x})^{3/2}\,(2n+1)^{3/2}\,\mathbb{E}\Big(\big|P_n(\boldsymbol{\omega}^T\boldsymbol{x})\big|^3\Big)}{\zeta_n^{1/2}},$$

where the sum is extended over all the integers n such that ζ_n is positive, G is the standard Gaussian cumulative distribution function, ξ is a constant between 0.4097 and 0.4748, and $\mathbb{E}\Big(\big|P_n(\boldsymbol{\omega}^T\boldsymbol{x})\big|^3\Big)$ does not depend on $\boldsymbol{x}$ and behaves as $\mathcal{O}(n^{-3/2})$ at large n. Now, in the four examples presented in Sect. 4.2, the simulated random field $\widetilde{Z}(\boldsymbol{x})$ has a unit variance, ε has a Rademacher distribution and $\{\zeta_n : n\in\mathbb{N}\}$ is the probability mass sequence of a shifted zeta distribution with parameter 2, so that $C(\boldsymbol{x},\boldsymbol{x})=1$, $\mathbb{E}(|\varepsilon|^3)=1$ and $\zeta_n^{-1/2}=\pi\,(n+1)/\sqrt{6}$. Accordingly:

$$\sup_{z\in\mathbb{R}}\left|\mathbb{P}\big(\widetilde{Z}(\boldsymbol{x})<z\big)-G(z)\right|\leq\frac{\xi}{L^{1/2}}\sum_n b_n(\boldsymbol{x})^{3/2}\,\tau_n,$$

with $\tau_n=(2n+1)^{3/2}\,\mathbb{E}\Big(\big|P_n(\boldsymbol{\omega}^T\boldsymbol{x})\big|^3\Big)\,\pi\,(n+1)/\sqrt{6}=\mathcal{O}(n)$ as $n\to+\infty$. Furthermore, one has:

- $b_n(\boldsymbol{x})=\mathcal{O}(n^{-2\nu(\boldsymbol{x})-1})$ with $\nu(\boldsymbol{x})\in[0.2,1.8]$ (Legendre-Matérn model);
- $b_n(\boldsymbol{x})=\mathcal{O}(a(\boldsymbol{x})^n)$ with $a(\boldsymbol{x})\in[0.1,0.9]$ (multiquadric model);
- $b_n(\boldsymbol{x})=\mathcal{O}\Big(\frac{a(\boldsymbol{x})^n}{n!}\Big)$ with $a(\boldsymbol{x})\in[0.1,8.0]$ (exponential-Bessel model);
- $b_n(\boldsymbol{x})=\mathcal{O}(a(\boldsymbol{x})^n\,n^{\nu(\boldsymbol{x})-1})$, with $a(\boldsymbol{x})\in[0.1,0.9]$ and $\nu(\boldsymbol{x})\in[1,19]$ (hypergeometric model).

As a result, in all the four cases, the sequence $\{b_n(\boldsymbol{x})^{3/2}\,\tau_n : n\in\mathbb{N}\}$ is summable, hence, the Berry–Esséen upper bound is finite and proportional to $L^{-1/2}$. By increasing L, it is possible to ensure that the distance between the marginal distribution of the simulated random field and a standard Gaussian distribution is less that any given positive threshold.

References

Adler RJ (1981) The geometry of random fields. Wiley & Sons, New York

Alegria A, Cuevas F, Diggle P, Porcu E (2018) A family of covariance functions for random fields on spheres. CSGB Research Reports, Department of Mathematics, Aarhus University, Aarhus

Alegría A, Emery X, Lantuéjoul C (2020) The turning arcs: a computationally efficient algorithm to simulate isotropic vector-valued Gaussian random fields on the d-sphere. Stat Comput. https://doi.org/10.1007/s11222-020-09952-8 In press

Alegría A, Porcu E, Furrer R, Mateu J (2019) Covariance functions for multivariate Gaussian fields evolving temporally over planet earth. Stoch Environ Res Risk Assess 33(8–9):1593–1608

Anh VV, Broadbridge P, Olenko A, Wang YG (2018) On approximation for fractional stochastic partial differential equations on the sphere. Stoch Environ Res Risk Assess 32(9):2585–2603

Arroyo D, Emery X (2017) Spectral simulation of vector random fields with stationary gaussian increments in d-dimensional euclidean spaces. Stoch Environ Res Risk Assess 31(7):1583–1592

Berg C, Porcu E (2017) From Schoenberg coefficients to Schoenberg functions. Constr Approx 45(2):217–241

Bingham N (1978) Tauberian theorems for Jacobi series. Proc Lond Math Soc 3(2):285–309

Brafman F (1951) Generating functions of Jacobi and related polynomials. Proc Am Math Soc 2(6):942–949

Castruccio S, Stein ML (2013) Global space-time models for climate ensembles. Ann Appl Stat 7(3):1593–1611

Cheng D, Xiao Y (2016) Excursion probability of Gaussian random fields on sphere. Bernoulli 22(2):1113–1130

Chilès J-P, Delfiner P (2012) Geostatistics: modeling spatial uncertainty, 2nd edn. John Wiley & Sons, New Jersey

de Fouquet C (1994) Reminders on the conditioning kriging. In: Armstrong M, Dowd P A (eds) Geostatistical simulations. Kluwer Academic, Dordrecht, pp 131–145

Devroye L (1986) Non-uniform random variate generation. Springer, New York

Emery X (2008) Statistical tests for validating geostatistical simulation algorithms. Compute Geosci 34(1):1610–1620

Emery X, Arroyo D (2018) On a continuous spectral algorithm for simulating non-stationary Gaussian random fields. Stoch Environ Res Risk Assess 32(4):905–919

Emery X, Arroyo D, Porcu E (2016) An improved spectral turning-bands algorithm for simulating stationary vector Gaussian random fields. Stoch Environ Res Risk Assess 30(7):1863–1873

Emery X, Lantuéjoul C (2006) TBSIM: A computer program for conditional simulation of three-dimensional Gaussian random fields via the turning bands method. Comput Geosci 32(10):1615–1628

Emery X, Lantuéjoul C (2008) A spectral approach to simulating intrinsic random fields with power and spline generalized covariances. Comput Geosci 12(1):121–132

Emery X, Porcu E (2019) Simulating isotropic vector-valued Gaussian random fields on the sphere through finite harmonics approximations. Stoch Environ Res Risk Assess 33(8–9):1659–1667

Fouedjio F, Desassis N, Rivoirard J (2016) A generalized convolution model and estimation for non-stationary random functions. Spat Stat 16:35–52

Gneiting T (2013) Strictly and non-strictly positive definite functions on spheres. Bernoulli 19(4):1327–1349

Gneiting T, Ševčíková H, Percival DB (2012) Estimators of fractal dimension: assessing the roughness of time series and spatial data. Stat Sci 27(2):247–277

Guella J, Menegatto V (2018) Unitarily invariant strictly positive definite kernels on spheres. Positivity 22(1):91–103

Guinness J, Fuentes M (2016) Isotropic covariance functions on spheres: some properties and modeling considerations. J Multivar Anal 143:143–152

Hansen LV, Thorarinsdottir TL, Ovcharov E, Gneiting T, Richards D (2015) Gaussian random particles with flexible Hausdorff dimension. Adv Appl Probab 47(2):307–327

Heaton M, Katzfuss M, Berrett C, Nychka D (2014) Constructing valid spatial processes on the sphere using kernel convolutions. Environmetrics 25(1):2–15

Hobolth A (2003) The spherical deformation model. Biostatistics 4(4):583–595
Jones RH (1963) Stochastic processes on a sphere. Ann Inst Math Stat 34:213–218
Jun M, Stein M (2008) Nonstationary covariance models for global data. Ann Appl Stat 2(4):1271–1289
Kent JT, Dryden IL, Anderson CR (2000) Using circulant symmetry to model featureless objects. Biometrika 87(3):527–544
Kucinskas AB, Turcotte DL, Huang J, Ford PG (1992) Fractal analysis of Venus topography in Tinatin Planitia and Ovda Regio. J Geophys Res Planets 97(E8):13635–13641
Lang A, Schwab C (2015) Isotropic Gaussian random fields on the sphere: regularity, fast simulation and stochastic partial differential equations. Ann Appl Probab 25(6):3047–3094
Lantuéjoul C (1994) Non conditional simulation of stationary isotropic multigaussian random functions. In: Armstrong M, Dowd P ,A (eds) Geostatistical simulations. Kluwer Academic, Dordrecht, pp 147–177
Lantuéjoul C (2002) Geostatistical simulation: models and algorithms. Springer, Berlin
Lantuéjoul C, Freulon X, Renard D (2019) Spectral simulation of isotropic Gaussian random fields on a sphere. Math Geosci 51(8):999–1020
Malyarenko A (2004) Abelian and Tauberian theorems for random fields on two-point homogeneous spaces. Theory Probab Math Stat 69:115–127
Mantoglou A, Wilson JL (1982) The turning bands method for simulation of random fields using line generation by a spectral method. Water Resour Res 18(5):1379–1394
Marinucci D, Peccati G (2011) Random fields on the sphere: representation, limit theorems and cosmological applications. Cambridge University Press, Cambridge
Matheron G (1973) The intrinsic random functions and their applications. Adv Appl Probab 5(3):439–468
Moller J, Nielsen M, Porcu E, Rubak E (2018) Determinantal point process models on the sphere. Bernoulli 24(2):1171–1201
Nott DJ, Dunsmuir WT (2002) Estimation of nonstationary spatial covariance structure. Biometrika 89(4):819–829
Olver FW, Lozier DM, Boisvert RF, Clark CW (2010) NIST handbook of mathematical functions. Cambridge University Press, Cambridge
Peron A, Porcu E, Emery X (2018) Admissible nested covariance models over spheres cross time. Stoch Environ Res Risk Assess 32(11):3053–3066
Porcu E, Alegria A, Furrer R (2018) Modeling temporally evolving and spatially globally dependent data. Int Stat Rev 86(2):344–377
Porcu E, Castruccio S, Alegria A, Crippa P (2019) Axially symmetric models for global data: a journey between geostatistics and stochastic generators. Environmetrics 30(1):e2555
Sánchez L, Emery X, Séguret S (2019) 5D geostatistics for directional variables: application in geotechnics to the simulation of the linear discontinuity frequency. Comput Geosci 133:104325
Schoenberg IJ (1942) Positive definite functions on spheres. Duke Math J 9(1):96–108
Schreiner M (1997) Locally supported kernels for spherical spline interpolation. J Approx Theory 89(2):172–194
Sedivy R, Mader RM (1997) Fractals, chaos, and cancer: do they coincide? Cancer Investig 15(6):601–607
Stoyan D, Stoyan H (1994) Fractals, random shapes, and point fields. John Wiley & Sons, Chichester
Zhou B, Wang J, Wang H (2017) Three-dimensional sphericity, roundness and fractal dimension of sand particles. Géotechnique 68(1):18–30
Ziegel J (2013) Stereological modelling of random particles. Commun Stat Theory Methods 42(7):1428–1442
Ziegel J (2014) Convolution roots and differentiability of isotropic positive definite functions on spheres. Proc Am Math Soc 142(6):2063–2077